JOURNAL OF AIRCRAFT
Vol. 39, No. 6, November–December 2002

Time-Linearized Transonic Computations Including Shock Wave Motion Effects

Eddie Ly*
National Aerospace Laboratory of Japan, Tokyo 181-0015, Japan
and
John Anthony Gear†
RMIT University, Melbourne, Victoria 3001, Australia

The effect of small perturbations on steady nonlinear transonic flowfields, in the context of two-dimensional flows governed by the general-frequency transonic small disturbance equation with nonreflecting far-field boundary conditions, is studied. Numerious existing time-linearized frequency-domain methods have failed to account for the shock wave motion that is known to occur. A time-linearized time-domain method, incorporating a procedure referred to as the shock jump correction procedure, is presented. This procedure allows one to account for correctly small-amplitude shock wave motions due to small unsteady changes in the airfoil boundary conditions. First harmonic pressure distributions and airloads for a NACA 64A006 airfoil with an oscillating quarter-chord flap are predicted and compared with those obtained from the time-linearized frequency-domain and nonlinear schemes and experiments. The comparisons reveal there are significant improvements in the time-domain results compared with the frequency-domain counterparts, specifically in the regions where the shock wave motions occur.

Nomenclature

C_{ℓ_δ}	=	first harmonic lift coefficient due to flap rotation, 1/rad
C_{m_δ}	=	first harmonic moment coefficient due to flap rotation, 1/rad
C_p	=	pressure coefficient
C_{pm}	=	mean pressure coefficient during oscillation
C_p^*	=	critical pressure coefficient
c	=	airfoil chord length
f	=	oscillation frequency, Hz
h	=	function defining instantaneous position of airfoil
Im	=	imaginary part of a complex-valued variable
$\imath$	=	$\sqrt{-1}$
k	=	reduced frequency or Strouhal number, $\omega c/U_\infty$
M_∞	=	freestream Mach number
N	=	number of steady solutions used to approximate the mean steady flowfield
p, q	=	constants used in grid shearing functions for streamwise direction
Re	=	real part of a complex-valued variable
t	=	nondimensional time
t_n	=	nondimensional discrete time, $n\Delta t$
U_∞	=	freestream fluid speed
$\boldsymbol{v}$	=	nondimensional fluid velocity vector
x, z	=	nondimensional Cartesian coordinates in streamwise and vertical directions, respectively
z_m, ζ_m	=	vertical extent of physical and computational domains, respectively
γ	=	ratio of specific heats (1.4 for ambient air)
ΔC_p	=	pressure coefficient perturbation
$\Delta\tilde{C}_p$	=	jump in first harmonic pressure coefficient across the airfoil normalized by the amplitude of flap oscillation
Δt	=	time step
$\Delta\delta$	=	amplitude of flap oscillation, deg
$\underset{z=0}{\Delta}\cdots$	=	jump in indicated quantity across the wake surface in physical domain
$\underset{\zeta=0}{\Delta}\cdots$	=	jump in indicated quantity across the wake surface in computational domain
δ	=	flap angle, deg
δ_m	=	mean flap angle during oscillation, deg
θ	=	shock angle relative to the positive z direction
ϑ	=	constants used in grid shearing functions
Λ	=	instantaneous shock wave position
Λ_t	=	shock wave speed
ξ, ζ	=	nondimensional computational coordinates in streamwise and vertical directions, respectively
ϕ	=	reduced potential
ϕ_m	=	mean reduced potential during oscillation
ψ	=	intermediate reduced potential used in the alternating direction implicit technique
ω	=	angular frequency, $2\pi f$, rad/s
$\langle\cdots\rangle$	=	jump in indicated quantity across the shock wave

Subscripts

o	=	oscillatory component of an one-harmonic time-linearized quantity
s	=	steady component of a time-linearized quantity or steady value
u	=	unsteady component of a time-linearized quantity

Superscripts

n	=	nth time level
$\pm$	=	upper/lower airfoil surface
-	=	average value of indicated quantity across the shock wave

Introduction

IN unsteady transonic flow, relatively small periodic changes in the boundary conditions can lead to substantial changes in the

Received 8 December 2001; revision received 18 June 2002; accepted for publication 29 June 2002.

*Science and Technology Agency/Japan Society for the Promotion of Science Fellow, Structures and Materials Research Center, Aeroelasticity Group, 6-13-1 Osawa, Mitaka.

†Senior Lecturer, Faculty of Applied Science, Department of Mathematics, G.P.O. Box 2476V.

aerodynamic loads and moments and so are of major concern (aeroelastic behavior) in aerodynamic design of aircraft that operate at transonic speeds. Transonic flows are characterized by the presence of adjacent regions of subsonic and supersonic flow, usually accompanied by shock waves.

In the past, there has been much activity in the development of computational methods for the analysis of time-linearized transonic aerodynamics. This activity was motivated by the need to supplement expensive and time consuming wind-tunnel tests with an affordable, fast, and efficient alternative. This paper presents a simple and fast scheme for computing time-linearized transonic flowfields, including the effects of shock wave motion, about an airfoil in unsteady motion of small amplitude. We consider the unsteady flow as a small perturbation on the mean (steady) flowfield, which results in a pair of coupled flow problems for the steady and first-order unsteady reduced potentials. The governing equation for the steady flow is the usual nonlinear transonic small disturbance (TSD) equation.[1,2] The first-order unsteady equation is linear and locally of mixed elliptic/hyperbolic type, depending on the nature of the steady solution. The time linearization process is performed in the time domain, rather than in the frequency domain, so that a procedure that we refer to as the shock jump correction procedure can be implemented. This procedure effectively corrects the solution values behind the shock, which in turn introduces the shock wave motion effects into the time-linearized solution.

For the past three decades, time-linearized equations were solved in the frequency domain by numerous researchers, including Hounjet,[3] Schippers and Hounjet,[4] and Traci et al.,[5,6] utilizing a variety of computational methods of different levels of complexity, where shock wave motion was neglected. In general, their results compare reasonably with the experimentally measured values, except in the regions where shock wave motion is anticipated. Even the most recent work from Greco et al.[7] for flutter and limit-cycle oscillation prediction neglect such significant effects, which can contribute substantially to the time-varying loads and moments. The only researchers, to our knowledge, who solved the time-linearized time-domain equations including the shock wave motion effects, are Fung et al.[8] However, their theory is based on the low-frequency TSD equation, hence applications of their scheme are restricted to transonic flows within the low-frequency range.

A suite of FORTRAN 90 codes, *TranFlow2D*, that are capable of generating isotropic and inviscid steady, nonlinear unsteady, and time-linearized frequency and time-domain solutions, for transonic flows over an oscillating airfoil was developed. In addition, a *Mathematica* package was developed for the grid-generation process and graphical postprocessing of the computed results. Time-linearized solutions for a NACA 64A006 airfoil with an oscillating quarter-chord flap, an AGARD aeroelastic configuration, will be presented and compared with experimental data.[9–11] The comparisons reveal significant improvements in the time-domain results over their frequency-domain counterparts, particularly in the critical regions where shock wave motion occurs.

Governing Equations and Boundary Conditions

This section briefly describes the governing equations and boundary conditions necessary for computing the steady, nonlinear unsteady, and time-linearized transonic flows over an aerofoil in motion. All angles are positive for trailing edge down, and moments are positive for nose up, taken about the airfoil quarter-chord point.

General-Frequency TSD Equation

A nearly planar wing is immersed in an unsteady, isentropic, and inviscid flow. The governing aerodynamic equation of motion is the unsteady general-frequency TSD equation,[1,12,13] which may be written in a convenient form as

$$M_\infty^2 \frac{\partial}{\partial t}(\phi_t + 2\phi_x) + \frac{\beta^2}{2\bar{u}} \frac{\partial}{\partial x} W^2 - \frac{\partial}{\partial z}\phi_z = 0 \tag{1}$$

where

$$W = \bar{u} - \phi_x \tag{2a}$$

$$\beta^2 = 1 - M_\infty^2 \tag{2b}$$

$$\bar{u} = \beta^2 \Big/ \left[M_\infty^2(\gamma + 1)\right] \tag{2c}$$

and $\phi_x = \partial\phi/\partial x$, etc. This equation is capable of capturing nonlinear flow phenomena, including irregular shock wave motion that was observed experimentally by Tijdeman.[14] The spatial coordinates (x, z), t, and ϕ have been nondimensionalized by c, c/U_∞, and $c\,U_\infty$, respectively. In nondimensional terms, the fluid velocity vector is given by $v = \nabla(x + \phi)$. Equation (1) is locally of elliptic/hyperbolic type, representing subsonic/supersonic flow when W is positive/negative, and its solution contains discontinuous jumps that approximate shock waves. Note that reduced potential means the potential of velocity disturbance from the freestream velocity and that $\bar{u}$ denotes the value of ϕ_x at sonic condition, that is, where local Mach number is one.

Boundary and Shock Jump Conditions

In the flowfield, nonreflecting boundary conditions derived from the theory of wave propagation[13,15] are employed at the far-field computational boundaries, and the Kutta condition is satisfied in the wake region behind the airfoil. The flow tangency boundary condition is imposed, in terms of airfoil slopes, on a flat mean surface approximation to the airfoil, as shown in Fig. 1. The airfoil lies on a $z = 0$ plane with leading (also the origin of the Cartesian coordinate

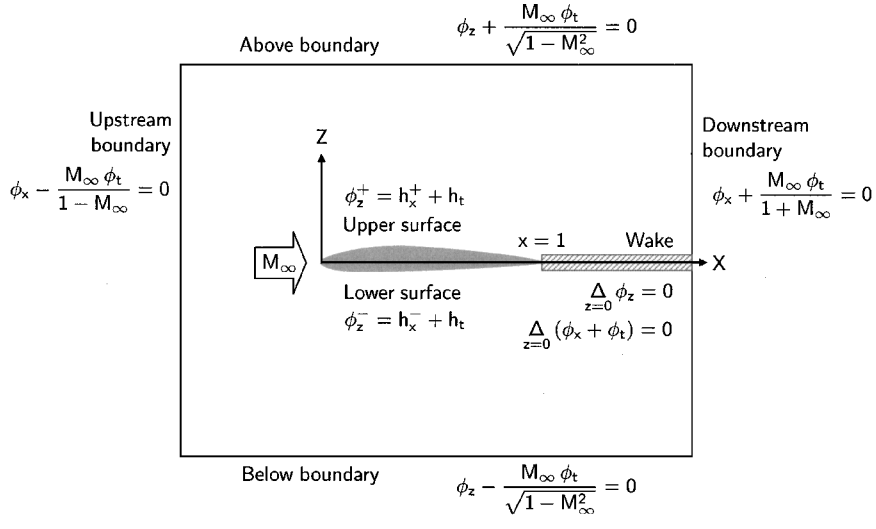

Fig. 1 Boundary conditions.

system) and trailing edges located at $x = 0$ and $x = 1$, respectively. The unbounded physical domain around an airfoil is truncated at some finite distance. Nonreflecting far-field boundary conditions are imposed and serve to simulate the disturbances that propagate outward from the airfoil to infinity. This allows the transonic solution to propagate through the artificial computational boundaries as if there are no boundaries present. Consequently, the far-field boundaries can be moved closer to the airfoil, and offer greater freedom in tradeoffs among grid density, accuracy, and computational cost. The airfoil functions required in the flow tangency boundary condition are obtained by least-square interpolation (using low-order polynomials) of the airfoil coordinates, taking into account of the square root behavior at the airfoil nose. Any shock wave that exists in the flowfield must satisfy the shock jump condition[2,8] derived from the conservation form of the governing equation (1), namely,

$$M_\infty^2\langle\phi_t + 2\phi_x\rangle\langle\phi_x\rangle\frac{\mathrm{d}\Lambda}{\mathrm{d}t} + \frac{\beta^2}{\bar{u}}(\bar{u} - \overline{\phi_x})\langle\phi_x\rangle^2 + \langle\phi_z\rangle^2 = 0 \qquad (3)$$

together with the condition derived from the assumption of irrotationality,

$$\theta = -\langle\phi_z\rangle/\langle\phi_x\rangle \qquad (4)$$

Mathematical Formulation and Numerical Procedures

The results of Fung et al.[8] for a one-dimensional model disclosed that the time-linearized results must be corrected for shock wave motion if they are to be consistently correct to the lowest order. This is accomplished by computing the shock wave motion in conjunction with the time-linearized solution process. Mathematical formulations for computing steady and time-linearized frequency-domain solutions will be briefy presented. Much attention is devoted to assessing the time-linearized time-domain method including the effects of shock wave motion.

Coordinate Transformation

To facilitate the use of high density of grid points surrounding the airfoil, without resolving to employment of a vast number of points, a smooth nonuniform computational mesh is constructed via an algebraic mapping process. In the mapping process the far-field boundaries are kept independent of the airfoil and aligned with respect to the freestream direction, so that both the physical and computational domains are contained within rectangular regions. The following transformation functions are employed:

$$x(\xi) = \begin{cases} \xi + \vartheta_1\xi^{2p+1} & \text{for} \quad \xi < 0 \\ \xi & \text{for} \quad 0 \le \xi \le 1 \text{ (airfoil)} \\ \xi + \vartheta_2(\xi - 1)^{2q+1} & \text{for} \quad \xi > 1 \text{ (wake)} \end{cases} \qquad (5a)$$

$$z(\zeta) = \vartheta_3 z_m\frac{\zeta}{\zeta_m} + (1 - \vartheta_3)z_m\left\{1 - \frac{\tanh[\vartheta_4 - \vartheta_4(\zeta/\zeta_m)]}{\tanh\vartheta_4}\right\} \quad \text{for} \quad 0 \le \zeta \le |\zeta_m| \qquad (5b)$$

The parameters ϑ_3 ($0 < \vartheta_3 < 1$) and ϑ_4 ($\vartheta_4 \neq 0$) provide the vertical grid point controls, and the slope of function (5b) is governed by ϑ_3 because, when ζ/ζ_m is close to zero, $z/z_m \approx \vartheta_3$. Here ϑ_4 controls the departure from the linear z/z_m vs ζ/ζ_m behavior. Small ϑ_4 values cause small departures from linearity, and departure from linearity will be small and occur for $\zeta \approx \zeta_m$ if $\vartheta_3 \approx 1$. To ensure there is no generation of reflections from internal grid points, because reflections sometimes do exist if grid stretching is excessive, ϑ_3 and ϑ_4 must be carefully chosen. Seidel et al.[16] show results indicating grid stretching in the vertical direction plays a predominant role in generating these reflections.

Steady Solution

The steady flow problem is governed by Eqs. (1–4), together with the steady version of the boundary conditions shown in Fig. 1, and the solution must satisfy the steady version of the shock relations [Eqs. (3) and (4)]. The finite difference solution procedure is based on the method of false transients,[1,2,17,18] in which an artificial first time derivative is appended to the steady TSD equation to incorporate temporal numerical dissipation. This artificial derivative is approximated by a generalized time difference rule, written in Padé form, and the resulting difference equation is approximately factorized.[1,2,12,19,20] Standard second-order accurate central difference rules are applied to all spatial derivatives, except for the nonlinear term, which is evaluated by the first- and second-order accurate Engquist–Osher type-dependent operators.[21] As the flow changes from subsonic to supersonic, Engquist–Osher operators smoothly change from central to upwind difference approximations, ensuring a smooth transition from subsonic to supersonic flow. Hence, entropy violating decompression shocks will not develop. As the flow changes from supersonic to subsonic, Engquist–Osher operators change to a proper shock point operator (see Ref. 22) satisfying the shock relations (3) and (4). Conservative differencing of the governing equation is preserved, an essential requirement for a proper description of shock waves. The resulting scheme is potentially fast because the solution process is fully vectorized and time-step cycling is used to enhance the rate of convergence.

Time-Linearized Frequency-Domain Solution

In the time-linearized approach, we assume unsteady disturbances are small relative to a fixed mean state. This assumption is reasonable as long as the disturbances are small, and if this is locally violated, such as in the shock trajectory, this assumption is still applicable provided the corresponding flow region is relatively small. The unsteady airfoil motion is assumed to consist of a steady component plus a small harmonically oscillating component. That is, neglecting higher harmonic terms in the unsteady responses, and for $|h_o| \ll 1$ and $|\phi_o| \ll |\phi_s|$, we let

$$h^\pm(\xi, t) = h_s^\pm(\xi) + \mathrm{Re}\left\{h_o(\xi)e^{\imath kt}\right\} \qquad (6a)$$

$$\phi(\xi, \zeta, t) = \phi_s(\xi, \zeta) + \phi_o(\xi, \zeta)e^{\imath kt} \qquad (6b)$$

Assumptions (6) have the advantage of suppressing the time dimension of the computation, but restrict the study to linear harmonic motions only, and result in two coupled equations. The airfoil thickness effect is included in the steady analysis, and the corresponding unsteady analysis is performed for an airfoil of vanishing thickness, but submerged in a steady reduced potential field. Substituting Eq. (6) into Eq. (1) with boundary conditions of Fig. 1, and separating the steady and oscillatory components, we find that ϕ_s satisfies the usual nonlinear steady TSD equation and corresponding steady boundary conditions and that ϕ_o satisfies

$$M_\infty^2k^2\phi_o - \imath 2M_\infty^2k\,\xi_x\frac{\partial\phi_o}{\partial\xi} + \frac{\beta^2}{\bar{u}}\xi_x\frac{\partial}{\partial\xi}W_s\,\xi_x\frac{\partial\phi_o}{\partial\xi} + \zeta_z\frac{\partial}{\partial\zeta}\zeta_z\frac{\partial\phi_o}{\partial\zeta} = 0 \qquad (7)$$

where

$$W_s = \bar{u} - \xi_x\frac{\partial\phi_s}{\partial\xi} \qquad (8)$$

subject to the following boundary conditions.

Downstream/upstream boundary:

$$\xi_x\frac{\partial\phi_o}{\partial\xi} \pm \frac{\imath M_\infty k}{1 \pm M_\infty}\phi_o = 0 \qquad (9a)$$

Above/below boundary:

$$\zeta_z\frac{\partial\phi_o}{\partial\zeta} \pm \frac{\imath M_\infty k}{\sqrt{1 - M_\infty^2}}\phi_o = 0 \qquad (9b)$$

Wake:

$$\underset{\zeta=0}{\Delta}\xi_x\frac{\partial\phi_o}{\partial\xi} + \imath\underset{\zeta=0}{\Delta}k\phi_o = 0 \qquad (9c)$$

$$\underset{\zeta=0}{\Delta}\frac{\partial\phi_o}{\partial\zeta} = 0 \qquad (9d)$$

Airfoil:

$$\zeta_z^{\pm}\frac{\partial \phi_o^{\pm}}{\partial \zeta} = \xi_x \frac{\partial h_o}{\partial \xi} + \imath k h_o \tag{9e}$$

Note that Eq. (7) is linear with respect to ϕ_o, but locally of the same mixed elliptic/hyperbolic type as Eq. (1) due to the dependence on ϕ_s through W_s. In general, ϕ_o is complex, thereby permitting phase shifts between the field quantities and the boundary disturbance.

The solution procedure for the frequency-domain problem is based on an iterative finite difference scheme.[2,23] The required solution for ϕ_s, which does not depend on ϕ_o, is solved independently, and the converged solution obtained is then used in the solution process for the corresponding ϕ_o. This approach has the benefit that ϕ_s need not be regenerated for each unsteady boundary disturbance or reduced frequency of interest. As usual, for a mixed elliptic/hyperbolic type equation, the second streamwise derivative in Eq. (7) is evaluated by the second-order accurate Engquist–Osher operators[21] (also see Ref. 13), whereas the rest of the spatial derivatives are evaluated by standard second-order accurate central difference rules.

Usually the actual steady-state flowfield at the mean position of an aerofoil motion is used to represent the mean (steady) flowfield in the time-linearized methods. In the time-domain computation, the shock wave motion effects are successfully included via the shock jump correction procedure. (This will be described in the next subsection.) However, when such a procedure is incorporated into the frequency-domain method, the resultant scheme becomes numerically unstable. This is due to the nonuniform convergence of the expansion in frequency near the shock. We also consider another representation of the mean flowfield, which is referred to as the mean steady flowfield throughout this paper, by taking a weighted average of the steady potentials at N different amplitudes of the airfoil motion.[3] Here we assume that the low-frequency change will become equivalent to a series of steady conditions for an attached flow as the rate of change is reduced. For example, for an oscillating flap motion, N steady potentials are computed for

$$\delta_j = \delta_m + \Delta\delta \cos(2\pi j/N) \qquad \text{for} \quad j = 1, 2, \ldots, N \tag{10}$$

and the mean steady flowfield is then obtained from

$$\phi_m = \frac{1}{N}\sum_{j=1}^{N} \phi_j \tag{11}$$

where ϕ_j is the potential solution obtained from solving the steady problem subject to the aerofoil disturbance δ_j of (10). In general, the mean steady flowfield [obtained from Eq. (11)] contains a discontinuous solution that spans the region in which the shock profile is likely to be influenced by viscous effects (see Fig. 2 and subsequent example). Therefore, this mean flowfield representation is usually better than taking the actual steady-state flowfield for the time-linearized frequency-domain computations. This distance also depends on the oscillation frequency of the airfoil motion and on the pressure distribution near the shock; see Ref. 14 for more details. However, we noticed that for the case studies considered here, where the reduced frequencies are high, the shock displacement is significantly small because the amplitude of shock wave motion[24] is proportional to $1/k$, and so the mean flowfield should be taken from a complete nonlinear unsteady solution of Eq. (1). This will be considered in our future work. Note that it is essential to have a well-defined mean (steady) flowfield because a good agreement on the steady pressure distribution is a prerequisite to obtain a good agreement on the unsteady pressure distribution for the time-linearized computations.

Time-Linearized Time-Domain Solution

This subsection describes a different approach in obtaining the time-linearized transonic solution, where instead of solving the equations in the frequency domain, we solve them in the time domain. There are two advantages to this approach: 1) Shock wave motion effects can be included in the time-linearized solution, so that the solution within the shock trajectory will be correctly predicted, and 2) no restrictions are imposed on the mode of airfoil motion, which can be simulated, because harmonic decomposition (6) is not utilized. The airfoil motion and reduced potential are time linearized (to first order) as follows, for $|h_u| \ll 1$ and $|\phi_u| \ll |\phi_s|$,

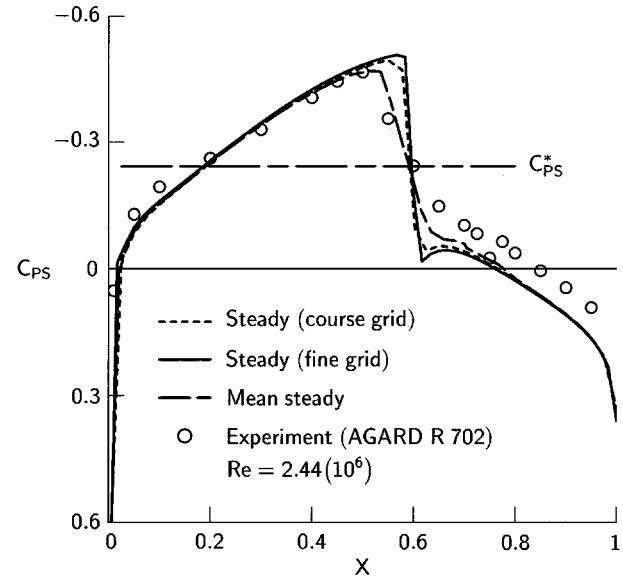

Fig. 2 Comparison of steady pressure distributions for the NACA 64A006 airfoil with a quarter-chord flap at $M_\infty = 0.88$ and $\delta_m = 0$ deg.

$$h^{\pm}(\xi, t) = h_s^{\pm}(\xi) + h_u(\xi, t) \tag{12a}$$

$$\phi(\xi, \zeta, t) = \phi_s(\xi, \zeta) + \phi_u(\xi, \zeta, t) \tag{12b}$$

Applying a similar process as described in the preceding subsection to obtain the relevant time-linearized equations, we find that ϕ_u satisfies

$$M_\infty^2 \frac{\partial^2 \phi_u}{\partial t^2} + 2M_\infty^2 \frac{\partial}{\partial t}\xi_x \frac{\partial \phi_u}{\partial \xi} - \frac{\beta^2}{\bar{u}}\xi_x \frac{\partial}{\partial \xi} W_s\, \xi_x \frac{\partial \phi_u}{\partial \xi} - \zeta_z \frac{\partial}{\partial \zeta}\zeta_z \frac{\partial \phi_u}{\partial \zeta} = 0 \tag{13}$$

subject to the same far-field and wake boundary conditions shown in Fig. 1 with ϕ_u replacing ϕ and the following airfoil boundary condition:

$$\zeta_z^{\pm}\frac{\partial \phi_u^{\pm}}{\partial \zeta} = \xi_x \frac{\partial h_u}{\partial \xi} + \frac{\partial h_u}{\partial t} \tag{14}$$

Equation (13) is linear with respect to ϕ_u, and it is locally of mixed elliptic/hyperbolic type, depending on the nature of the steady solution. The linearity of Eq. (13) makes the computation effort required to obtain a solution much less than the effort required to obtain a solution of the nonlinear TSD equation [Eq. (1)].

Our numerical experiments[2,13,23] and experiments of Tijdeman and Schippers[10] and Tijdeman[14] all have indicated that an accurate representation of shock wave motion is of great importance for transonic flow simulations. The experiments reveal that for two-dimensional small perturbation transonic flows the shock waves that usually occur are nearly normal to the flow direction. Therefore, we can assume that if the steady flowfield has a shock, then this shock may be represented by a normal shock wave. The shock wave motion is explicitly treated as

$$\Lambda(t) = \Lambda_s + \Lambda_u(t) \tag{15}$$

and $\phi[\Lambda(t), \zeta, t]$ is expanded using a Taylor series expansion about $\xi = \Lambda_s$,

$$\phi[\Lambda(t), \zeta, t] = \sum_{j=0}^{\infty} \frac{\Lambda_u^j}{j!}\left(\xi_x \frac{\partial}{\partial \xi}\right)^j \phi \tag{16}$$

Substituting relations (12b) and (15) into the preceding series, imposing the condition of no circulation around infinitesimal paths

threading the shock front, and neglecting higher-order terms in Λ_u provides

$$\langle \phi_s(\Lambda_s, \zeta)\rangle = 0 \tag{17a}$$

$$\langle \phi_u(\Lambda_s, \zeta, t)\rangle = -\Lambda_u\left\langle \xi_x \frac{\partial \phi_s}{\partial \xi}\right\rangle \tag{17b}$$

Note that $\langle \xi_x \partial\phi_s/\partial\xi\rangle$ represents the jump in C_{ps} across the shock at $x(\xi) = \Lambda_s$. Another relation that allows us to compute Λ_u knowing the ϕ_u value is needed before Eq. (17b) can be applied. This important relation stems from the time linearization of Eq. (3). For a normal shock wave, Eqs. (3) and (4) reduce to

$$\frac{\mathrm{d}\Lambda}{\mathrm{d}t} = \frac{\beta^2(\overline{\xi_x\phi_\xi} - \bar{u})\langle \xi_x \phi_\xi\rangle}{\bar{u} M_\infty^2 \langle \phi_t + 2\xi_x \phi_\xi\rangle} \tag{18a}$$

$$\theta = 0 \tag{18b}$$

Because we have treated the shock as normal, Eq. (18a) is computed at one ζ location (as suggested by Fung et al.[8]) at the airfoil surface. Time linearizing Eq. (18a) using Eqs. (12b) and (15) shows that $\bar{C}_{ps} = C_p^* = -2\bar{u}$ and that the time-linearized shock speed is given by

$$\frac{\mathrm{d}\Lambda_u}{\mathrm{d}t} = \frac{\beta^2}{2\bar{u}M_\infty^2}\overline{\xi_x \frac{\partial \phi_u}{\partial \xi}} \tag{19}$$

The solution is computed utilizing a noniterative alternating directional implicit (ADI) technique, where the solution values behind the shock are corrected to incorporate the shock wave motion effects. We anticipate that this shock jump correction procedure will improve the numerical results in the regions where shock wave motion occurs. In the ADI technique, the solution marches forward in time from its initial steady state to subsequent time levels in a two-step process from time level t_n to t_{n+1}. Intermediate values, $\psi(\xi, \zeta, t)$, are computed at the midpoint of each time interval. Equation (13) and all associated unsteady boundary conditions are discretized at time level $t_{n+\frac{1}{2}}$, which is the midpoint of time levels t_n and t_{n+1}. The first and second time derivatives are evaluated by trapezoidal rule and second-order accurate nonstandard forward approximation involving ϕ_u^{n-2}, ϕ_u^{n-1}, ϕ_u^n, and ϕ_u^{n+1} values, respectively. Likewise, the vertical derivative is averaged between the values at time level t_n and t_{n+1}, resulting in

$$\frac{M_\infty^2}{2(\Delta t)^2}\left(3\phi_u^{n+1} - 7\phi_u^n + 5\phi_u^{n-1} - \phi_u^{n-2}\right) + \frac{2M_\infty^2}{\Delta t}\xi_x \frac{\partial}{\partial \xi}\left(\phi_u^{n+1} - \psi\right)$$

$$+ \frac{2M_\infty^2}{\Delta t}\xi_x \frac{\partial}{\partial \xi}\left(\psi - \phi_u^n\right) = \frac{\beta^2}{\bar{u}}\xi_x \frac{\partial}{\partial \xi} W_s\, \xi_x \frac{\partial \psi}{\partial \xi} + \zeta_z \frac{\partial}{\partial \zeta}\zeta_z \frac{\partial \phi_u^n}{\partial \zeta}$$

$$+ \frac{1}{2}\zeta_z \frac{\partial}{\partial \zeta}\zeta_z \frac{\partial}{\partial \zeta}\left(\phi_u^{n+1} - \phi_u^n\right) \tag{20}$$

In the first half-step, ψ is computed along $\zeta = \text{const}$ lines using

$$\frac{2M_\infty^2}{\Delta t}\xi_x \frac{\partial \psi}{\partial \xi} - \frac{\beta^2}{\bar{u}}\xi_x \frac{\partial}{\partial \xi} W_s\, \xi_x \frac{\partial \psi}{\partial \xi} = \frac{2M_\infty^2}{\Delta t}\xi_x \frac{\partial \phi_u^n}{\partial \xi} + \zeta_z \frac{\partial}{\partial \zeta}\zeta_z \frac{\partial \phi_u^n}{\partial \zeta} \tag{21}$$

coupled with the computation of new ψ values behind the shock obtained from Eq. (19). In Eq. (13) and subsequent equations, $\partial\phi_u^n/\partial\xi$ denotes the value of $\partial\phi_u/\partial\xi$ at time level t_n, etc. We basically write Eq. (17b) at time level $t_{n+\frac{1}{2}}$, differentiate it with respect to time, and follow by inserting Eq. (19) for the shock speed term. The first time derivative is then evaluated by a first-order accurate forward difference rule, and the $\overline{\xi_x \psi_\xi}$ term is approximated at time level t_n. With the shock location dictated by the shock point operator, the ψ values ahead of and behind the shock can be expressed by a Taylor series expansion, and we obtained

$$\langle \psi\rangle = \langle \phi_u^n\rangle - \frac{\Delta t\, \beta^2}{2\bar{u}M_\infty^2}\left\langle \xi_x \frac{\partial \phi_s}{\partial \xi}\right\rangle \overline{\xi_x \frac{\partial \phi_u^n}{\partial \xi}} \tag{22}$$

With the ψ values determined, the second half-step follows, computing ϕ_u^{n+1} values along the $\xi = \text{const}$ lines via

$$\frac{3M_\infty^2}{2(\Delta t)^2}\phi_u^{n+1} + \frac{2M_\infty^2}{\Delta t}\xi_x \frac{\partial \phi_u^{n+1}}{\partial \xi} - \frac{1}{2}\zeta_z \frac{\partial}{\partial \zeta}\zeta_z \frac{\partial \phi_u^{n+1}}{\partial \zeta}$$

$$= \frac{M_\infty^2}{2(\Delta t)^2}\left(7\phi_u^n - 5\phi_u^{n-1} + \phi_u^{n-2}\right) + \frac{2M_\infty^2}{\Delta t}\xi_x \frac{\partial \psi}{\partial \xi}$$

$$- \frac{1}{2}\zeta_z \frac{\partial}{\partial \zeta}\zeta_z \frac{\partial \phi_u^n}{\partial \zeta} \tag{23}$$

in conjunction with the updated $\langle \phi_u\rangle$ values,

$$\left\langle \phi_u^{n+1}\right\rangle = \langle \psi\rangle \tag{24}$$

In Eqs. (21) and (23), the first streamwise and all vertical derivatives are evaluated by standard second-order accurate, upwind and central rules, respectively. Second-order accurate Engquist–Osher operators[21] (see also Ref. 22) are applied to the second streamwise derivative in Eq. (21). It is necessary to introduce the boundary values from the boundary conditions for ψ that are compatible with the interior algorithms corresponding to Eqs. (21) and (23). An appropriate strategy for the inclusion of the boundary values will not be discussed in this paper. The final finite difference scheme is globally second-order accurate in the spatial and time dimensions, except in the regions where shock wave motion occurs, in which the time dimension reduces to first-order accuracy. For a mixed flow, numerical instabilities may be generated by the shock excursion, hence restricting the use of large time steps for both accuracy and stability in the scheme. The solution procedure outlined here effectively corrects the ϕ_u values for shock wave motions as the solution progresses. The correction procedure disregards the actual variation in ϕ_u and, thus, is only able to account for shock wave motions provided they remain small. The shock displacement is easily determined simultaneously using relations (15) and (17b).

Results and Discussion

Time-linearized results have been computed for an NACA 64A006 airfoil experiencing harmonic flap motions at zero angle of attack. To confirm the validity of the time-linearized computations, both the time-linearized and nonlinear schemes were used to compute the solutions to two case studies. Experimental results are also used to provide the physical insights of the flows. The nonlinear unsteady solution is obtained by solving Eq. (1) based on the scheme of Ref. 13. The maximum thickness of this symmetrical airfoil is 6%, located at about 38% chord, and the hinge axis of the quarter-chord flap is located at 75% chord with gap width of 0.1 mm. Computations are performed for symmetrical flow [case 1, AGARD, $M_\infty = 0.88$, $k = 0.468$, $\delta_m = 0$ deg, and $\Delta\delta = 1$ deg] and antisymmetrical flow [case 2, National Aerospace Laboratory (NLR), $M_\infty = 0.872$, $k = 0.47$, $\delta_m = 0.86$ deg, and $\Delta\delta = 0.6$ deg] conditions. Case 1 uses a standard AGARD aeroelastic configuration, where the airfoil profile coordinates and experimental data are obtained from AGARD reports,[9,11] and case 2 uses an NLR configuration, employing the standard NACA 64A006 airfoil of Ref. 25. The airfoil profile used in the first case has been augmented by eight new coordinates in the nose region (from 0.05 to 0.4% chord), and the nose radius of the airfoils for both cases remain unchanged at 0.246% chord. Predicted results for case 2 will be compared with the experimental data from an NLR report.[10] Although the two sets of profile coordinates are for the same airfoil, because of the sensitivity of transonic computations to airfoil slopes, it is important to clearly distinguish which sets are used in the computation processes. Note that k is scaled with c, rather than $c/2$ as usually done and that before the time-linearized computations steady-state flowfields, representation of the mean flowfields, are computed using a nonlinear steady solver as described in the subsection on steady solution.

It is convenient to restrict the discussion to pressure distributions and resulting forces and moments because it is the pressures that are actually measured. Once reduced potentials are determined, pressure coefficients are computed from

$$C_p(\xi, \zeta, t) = -2\xi_x \phi_\xi - 2\phi_t \tag{25a}$$

$$C_p(\xi, \zeta, t) = C_{pm}(\xi, \zeta) + \Delta C_p(\xi, \zeta, t) \tag{25b}$$

$$C_p(\xi, \zeta, t) = C_{ps}(\xi, \zeta) + \mathrm{Re}\left\{C_{po}(\xi, \zeta) e^{\imath k t}\right\} \tag{25c}$$

$$C_p(\xi, \zeta, t) = C_{ps}(\xi, \zeta) + C_{pu}(\xi, \zeta, t) \tag{25d}$$

where

$$C_{ps} = -2\xi_x \frac{\partial \phi_s}{\partial \xi} \tag{26a}$$

$$C_{po} = -2\xi_x \frac{\partial \phi_o}{\partial \xi} - \imath 2k\phi_o \tag{26b}$$

$$C_{pu} = -2\xi_x \frac{\partial \phi_u}{\partial \xi} - 2\frac{\partial \phi_u}{\partial t} \tag{26c}$$

Relations (25b) corresponds to the nonlinear unsteady pressure and Eqs. (25c) and (25d) correspond to the time-linearized frequency- and time-domain pressures, respectively. Locally supersonic flow is represented by C_p/C_p^* value greater than one. In all computations, 9000 grid points are employed to discretize the grid with the far-field computational boundaries located at a distance of four chord lengths from the airfoil (Fig. 1). In the streamwise direction, 15 grid points are allocated to the upstream region, 60 for the airfoil (referred to as the fine grid configuration, discussed later), and 15 for the wake region, a total of 90 grid points. In the vertical direction, 50 grid points are allocated to the flow regions above and below the aerofoil. The p, q, ϑ_3, and ϑ_4 values of the shearing functions (5) are 2, 2, 0.2, and 5, respectively, with ϑ_1 and ϑ_2 calculated from the p and q values. Reflections from internal grid points were not observed. For the time-domain solutions, computations were started from the initial steady state, and continued for six oscillation cyles, at which time the solution becomes periodic after four cycles.

A study of grid dependence is carried out by computing several solutions using the same grid configuration as mentioned earlier, but allocating 30, 35, 40, 45, 50, 55, and 60 grid points to the airfoil. It was found that using 40 grid points is adequate, and using more than 40 produces small improvements in the results near the shock wave. The steady pressure distributions for case 1 are presented in Fig. 2, and the jump in first harmonic pressure distributions across the airfoil follow in Figs. 3 and 4. Figures 3 and 4 show the jump in first harmonic pressure distributions, normalized by $\Delta\delta$, across the NACA 64A006 airfoil with a harmonically oscillating quarter-chord flap at $M_\infty = 0.88$, $k = 0.468$, $\delta_m = 0$ deg, and $\Delta\delta = 1$ deg. Figure 2 illustrates that there is a very small improvement in the result using the fine grid configuration over that of the course grid configuration (40 grid points for the aerofoil). The computed steady shock profile is sharper than that obtained from the experiment, where the shock is smeared due to the boundary layer. In an effort to obtain a similar profile to the experimental results (without resorting to the inclusion of boundary-layer effects), a mean steady flowfield is constructed by averaging nine steady solutions at flap angles of δ_m, $\delta_m \pm \frac{1}{4}\Delta\delta$, $\delta_m \pm \frac{1}{2}\Delta\delta$, $\delta_m \pm \frac{3}{4}\Delta\delta$, and $\delta_m \pm \Delta\delta$. All computed and experimental results compare very well in the region upstream of the shock wave, all give the same steady shock position, and supersonic points appear in between about 19 and 59.7% chord. However, small discrepancies exist in the region behind the shock. We believe this is partly due to the boundary-layer effect, which is not taken into account in the present theory and also due to the real shock excursion being smaller than for the averaging procedure used here. The steady flowfield is symmetric because we are dealing with zero angle of attack and zero mean flap angle, and the shock displacements and unsteady pressures on the upper and lower airfoil surfaces are equal in magnitude, but differ by 180 deg in phase angle.

To assist in the comparison of the time-domain results, an approximating trace of the responses in the form of a truncated Fourier series with only one harmonic is fitted to the result by a least-squares procedure. The fitted parameters are then written in complex-valued

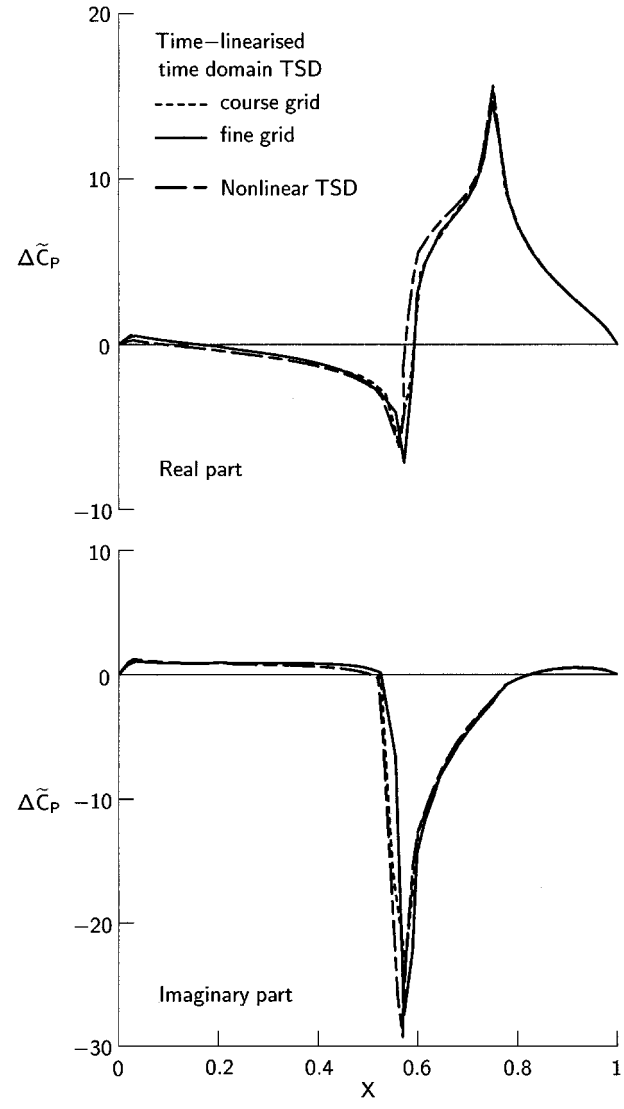

Fig. 3 Comparison between the time-linearized time-domain (using course and fine grids) and full nonlinear TSD results.

form, normalized by $\Delta\delta$, so that the real and imaginary parts of $\Delta\tilde{C}_p$ per radian, where $\Delta\tilde{C}_p = (\Delta C_p^+ - \Delta C_p^-)/\Delta\delta$, can be extracted and plotted as shown in Figs. 3 and 4. The real and imaginary parts represent the in-phase and in-quadrature solution, respectively. Figure 3 compares the time-linearized time-domain results using course and fine grid configurations to those obtained from the nonlinear scheme of Ref. 13. Apart from the small differences in the pressure distributions, the comparison in general is very good, especially the well-captured pressure peaks due to the steady shock (first peak) and flap hinge (second peak), hence indicating that the shock wave motion effects are correctly introduced into the time-linearized time-domain scheme by the shock jump correction procedure. Further comparison is made in Fig. 4 between the time-linearized frequency-domain results employing the actual and mean steady flowfields to represent the mean flowfield and those measured in the experiment. We observe that in the regions away from the shock trajectory, the comparison of the results show good qualitative agreement, although in the shock region only the time-domain method can accurately predict the dip in the real pressure part. The computed airloads are obtained from the pressures by integration (using trapezoidal rule) of the separate real and imaginary parts and compared with the experimental[11] values in Table 1. The time-domain method predicts the lift coefficient more accurately, with respect to those computed by the nonlinear scheme, than the frequency-domain methods, whereas for the moment coefficient, the real part is astonishingly well predicted by all methods.

Table 1 Comparison of first harmonic lift and moment coefficients due to flap rotation

Method	Re C_{ℓ_δ}	Im C_{ℓ_δ}	Re C_{m_δ}	Im C_{m_δ}
		Case 1		
Experiment	0.579	−0.479	0.757	−0.327
Nonlinear	0.614	−0.553	0.730	−0.401
TLTD	0.599	−0.511	0.723	−0.375
TLFD (S)[a]	0.723	−0.352	0.740	−0.335
TLFD (MS)[b]	0.735	−0.419	0.740	−0.371
		Case 2		
Experiment	0.629	−0.558	0.805	−0.375
Nonlinear	0.679	−0.507	0.744	−0.436
TLTD	0.655	−0.516	0.762	−0.414
TLFD (S)	0.698	−0.360	0.727	−0.334
TLFD (MS)	0.703	−0.387	0.729	−0.347

[a]Using steady flowfield. [b]Using mean steady flowfield.

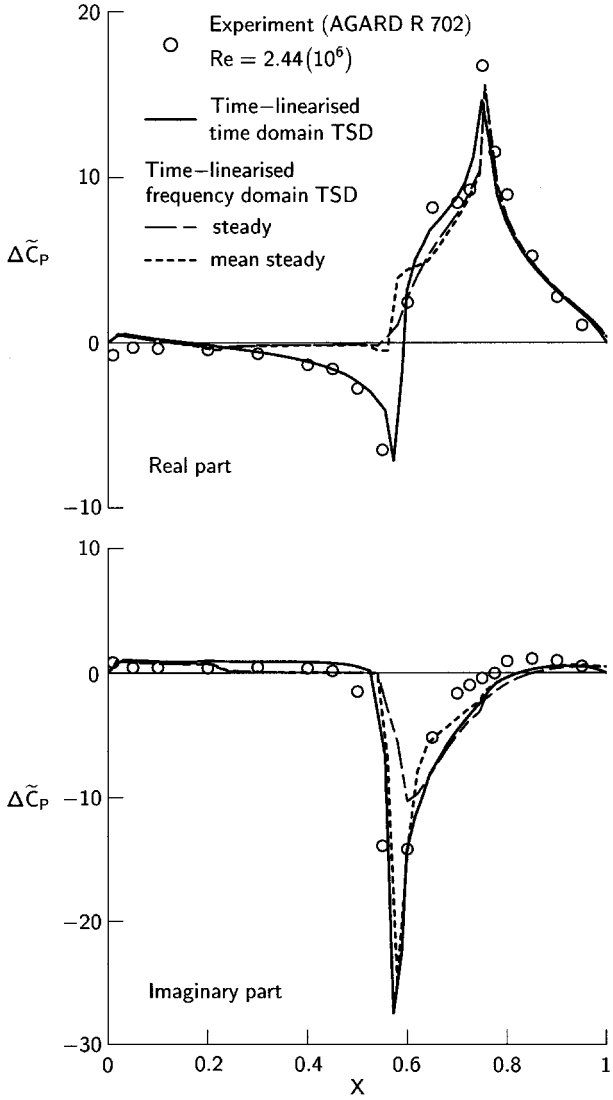

Fig. 4 Comparison between the time-linearized TSD and experimental results.

In case 2, we have an antisymmetrical flowfield with steady upper surface shock located farther downstream than that on the lower surface (Fig. 5). Five steady solutions at flap angles δ_m, $\delta_m \pm \frac{1}{2}\Delta\delta$, and $\delta_m \pm \Delta\delta$ are utilized to construct the mean steady flowfield for the frequency-domain computation. Supersonic regions are evident on both airfoil surfaces, with the larger region on the upper surface. The supersonic regions start at 19.3% chord and are terminated by a shock at 63.5 and 52.6% chord. Figure 5 reveal a small improvement in the mean steady solution in predicting the

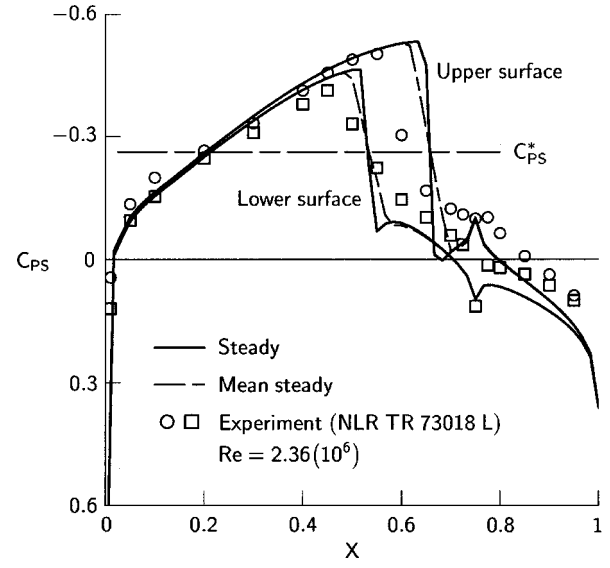

Fig. 5 Comparison of steady pressure distributions for the NACA 64A006 airfoil with a quarter-chord flap at $M_\infty = 0.872$ and $\delta_m = 0.86$ deg.

pressure distribution in the shock regions. Note that viscous effects on the pressure distribution in the shock region are still crucial, and this will be considered in our future work. The jump in first harmonic pressure distributions across the airfoil is presented and compared in Figs. 6 and 7. Figures 6 and 7 show the jump in first harmonic pressure distributions, normalized by $\Delta\delta$, across the NACA 64A006 airfoil with a harmonically oscillating quarter-chord flap at $M_\infty = 0.872$, $k = 0.47$, $\delta_m = 0.86$ deg, and $\Delta\delta = 0.6$ deg. The time-linearized time-domain result is still acceptable even though small differences with that of the nonlinear result (as shown in Fig. 6) exist because both methods give the same trend of pressure distributions along the airfoil surfaces. Significant improvements are achieved by the time-domain method in predicting the real pressure peak due to the steady shocks (Fig. 7). Table 1 shows a comparison of the aerodynamic coefficients, where we see satisfactory agreement among all results. The time-domain results compare most favorably to the nonlinear results. Consequently, the main conclusion we derive from these case studies is that it is essential to consider shock wave motion in computing time-linearized solutions if we are to determine the effects of small unsteady perturbations correctly to the lowest order.

The loci of the time-linearized shock wave motions and those predicted by the nonlinear scheme are compared in Figs. 8 and 9 (last cycle only) for cases 1 and 2, respectively. Inspection of Fig. 8 reveals that the shocks travel over approximately 3.4% (time-linearized result) and 3.8% (nonlinear result) of the chord with the steady shock location as the neutral position. The shock displacements on the upper and lower airfoil surfaces are equal in magnitude, but out of phase by 180 deg. Good agreement exists for most part of the shock trajectory, except during the times when the flap approaches the maximum angles, whereas, for case 2, the upper shock travels over a distance of 1.1% (time-linearized result) and 1.4% (nonlinear result) chord, and the lower shock travels about 4.0% and 3.5% chord. For these flow conditions (high k values) the resultant shock wave motions are very small, and the shocks move linearly with the flap motion with small phase lags.

Table 2 compares the computation time per iteration used by the steady and time-linearized frequency-domain (TLFD) methods, and computation time per time step for the nonlinear and time-linearized time-domain (TLTD) methods, together with the absolute computation time per grid point. All computations were done on an IBM Thinkpad T22 notebook with an Intel Pentium III processor of speed about 1 GHz, Microsoft Windows 2000 Professional operating system with 393 MB of physical memory and 1337 MB of virtual memory. The time-domain method requires about 35% less time to that required by the nonlinear method for each time step, and the

Table 2 Comparison of computation times

Method	Computation time per iteration or time step, 10^{-3} s	Computation time per grid point, 10^{-6} s
Steady	17.846	1.947
Nonlinear	35.117	3.630
TLTD	22.197	2.425
TLFD	457.741	50.016

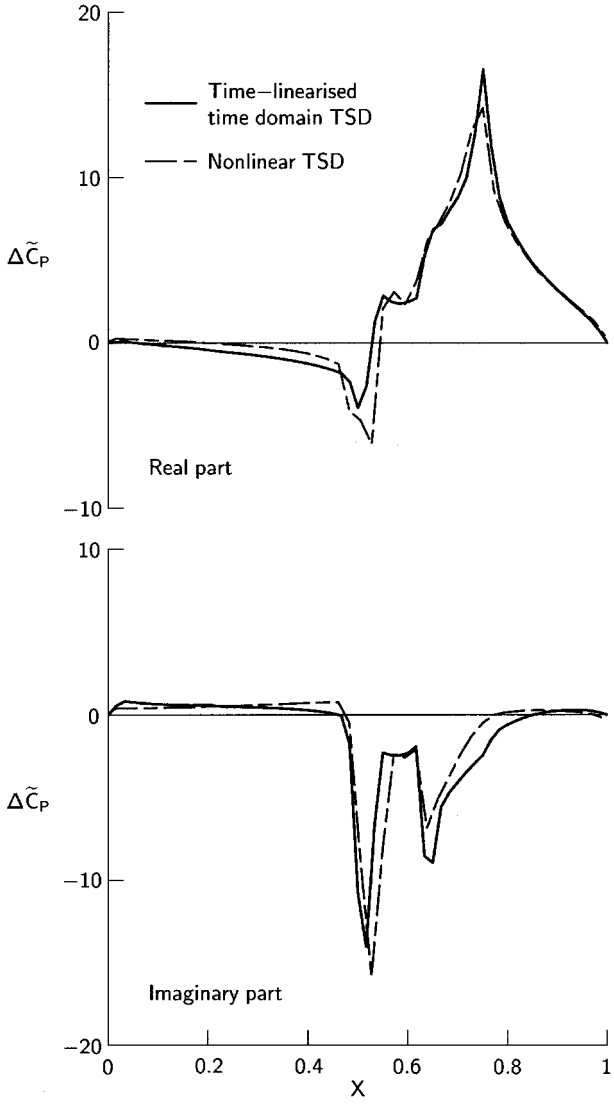

Fig. 6 Comparison between the time-linearized time-domain and full nonlinear TSD results.

number of time steps required for a periodic solution is also much smaller. Thus, the actual saving in the total computation time by the time-domain method for a periodic solution is greater than 35%. The frequency-domain method uses about 0.4577 s per iteration, which is 13 times more than that required by the nonlinear method for each time step, because the scheme solves an unfactorized equation system, involving direct inversion of a complex-valued banded block diagonal coefficient matrix. However, the frequency-domain solution, in general, converges in less than 50 iterations, and only one matrix inversion is required, and so the required total time will be much smaller than that required by the nonlinear method for a solution. Overall, the comparison shows that the TLTD method is efficient, and accurate transonic solutions can be generated in an acceptable turnaround time on current high-speed personal computers. Note that the main objective in developing the TranFlow2D suite of codes is to provide researchers with an efficient tool for performing

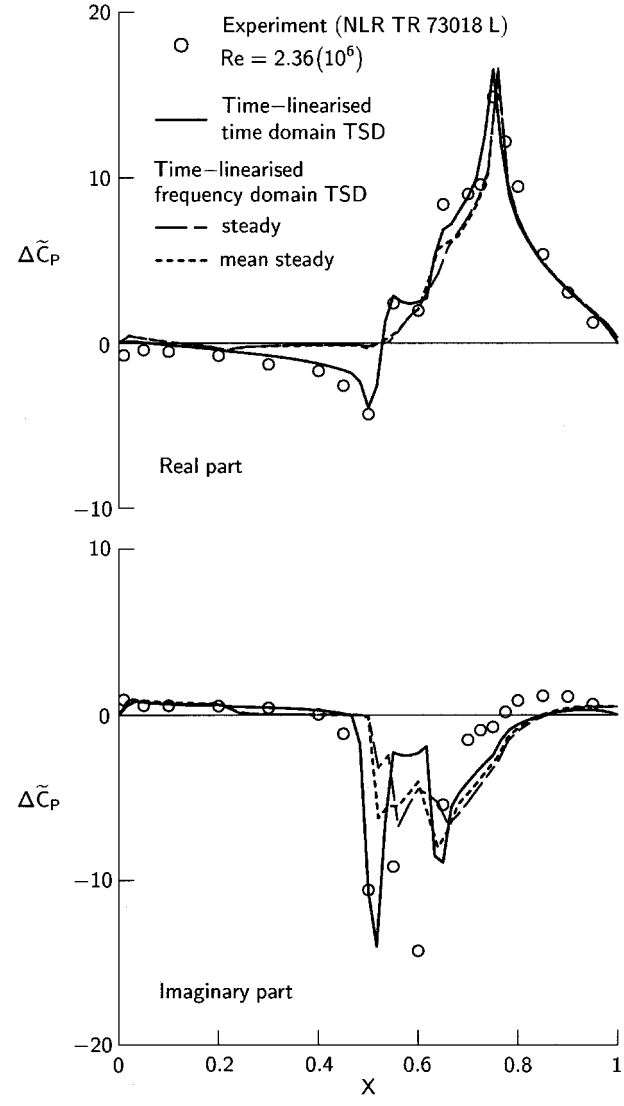

Fig. 7 Comparison between the time-linearized TSD and experimental results.

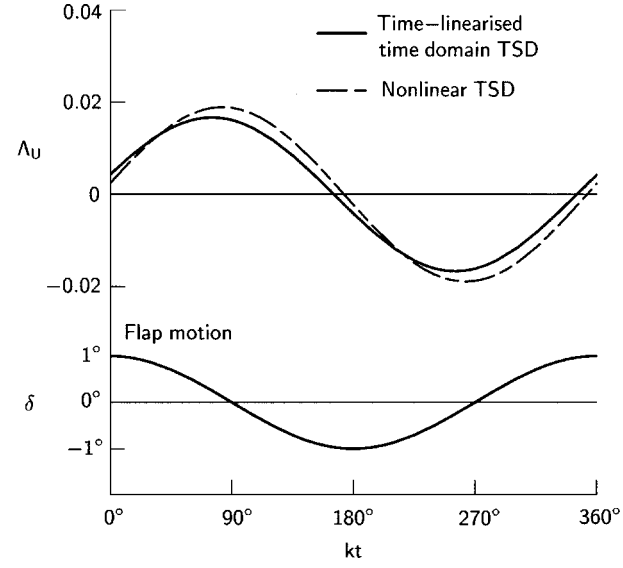

Fig. 8 Comparison of predicted shock trajectory for the NACA 64A006 airfoil with a harmonically oscillating quarter-chord flap at $M_\infty = 0.88, k = 0.468, \delta_m = 0$ deg, and $\Delta\delta = 1$ deg.

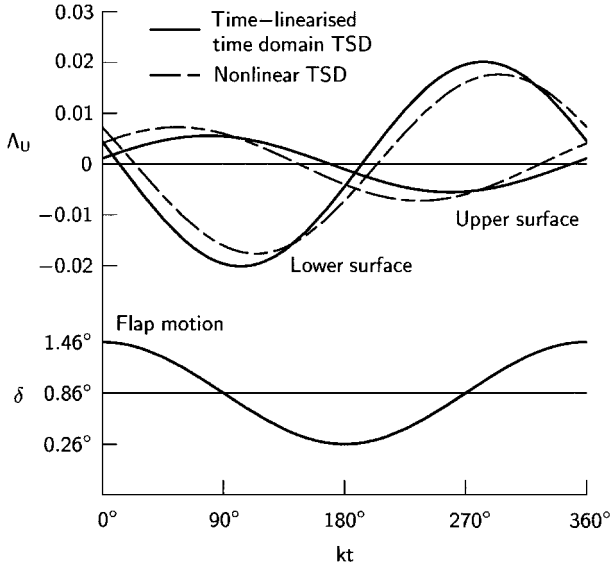

Fig. 9 Comparison of predicted shock trajectory for the NACA 64A006 airfoil with a harmonically oscillating quarter-chord flap at $M_\infty = 0.872$, $k = 0.47$, $\delta_m = 0.86$ deg, and $\Delta\delta = 0.6$ deg.

transonic aeroelastic analysis, and to provide students with a hands-on tool for study of and experience with aerodynamic computations.

Conclusions

An effective treatment of unsteady transonic flow as a small perturbation about the nonlinear steady flowfield is presented. An accurate and efficient procedure for computing TLTD transonic flows, including shock wave motions, has been developed and applied to a NACA 64A006 airfoil with an oscillating quarter-chord flap. Computed results compare reasonably well with the nonlinear solution and experimental data except for some small quantitative discrepancies that exist in the region behind the shock. We suspect this would be related mainly to the viscous effects that are not accounted for in the present theory and also are due to the interferences occuring while measuring the experimental values. The case studies presented signified that, for unsteady transonic flow, which is dominated by the shock wave motion effects, the time-domain method with shock jump correction procedure is preferred over the frequency-domain counterpart because the frequency-domain method is not capable of predicting the solution in the shock regions. The time-domain method also demonstrates the importance of proper modeling of the shock wave motion to obtain accurate time-linearized transonic solutions. The solutions can be obtained in acceptable turnaround time on current high-performance personal computers, hence making it an ideal tool for peforming two-dimensional transonic aeroelastic analysis and for students to experience aerodynamic computations. Finally, the theory and solution method have been demonstrated to be successful, in the sense that the method could be used to provide input for aeroelastic computations for which only infinitesimal amplitude motions need be considered. There is a future potential for a three-dimensional version as a fast method to be used for flutter prediction.

Acknowledgments

This research was supported under the first author's Science and Technology Agency/Japan Society for the Promotion of Science (JSPS). Fellowship Program, commissioned by the Japan Science and Technology Corporation and JSPS. The authors would like to thank the National Aerospace Laboratory of Japan, Tokyo, Japan, for being the host institute and making research facilities available to the first author.

References

[1]Ly, E., "Improved Approximate Factorisation Algorithm for the Steady Subsonic and Transonic Flow over an Aircraft Wing," *Proceedings of the 21st Congress of the International Council of the Aeronautical Sciences*, Paper A98-31699, Sept. 1998.

[2]Ly, E., Gear, J. A., and Phillips, N. J. T., "Simulated Shock Motion Using a Time-Linearised Transonic Code," *Proceedings of the 3rd Biennial Engineering Mathematics and Applications Conference*, Inst. of Engineers of Australia and Australian and Newzealand Industrial and Applied Mathematics, Adelaide, Australia, July 1998, pp. 331–334.

[3]Hounjet, M. H. L., "NLR Inviscid Transonic Unsteady Loads Prediction Methods in Aeroelasticity," *Transonic Unsteady Aerodynamics and Aeroelasticity*, CP-507, AGARD, March 1992, pp. 12.1–12.16.

[4]Schippers, H., and Hounjet, M. H. L., "Two Complementary Approaches to Transonic Potential Flow About Oscillating Airfoils," *Journal of Aircraft*, Vol. 25, No. 5, 1988, pp. 395–398.

[5]Traci, R. M., Albano, E. D., and Farr, J. L., Jr., "Small Disturbance Transonic Flows about Oscillating Airfoils and Planar Wings," AFFDL TR-75-100, Air Force Flight Dynamics Lab., Wright–Patterson AFB, OH, Aug. 1975.

[6]Traci, R. M., Albano, E. D., and Farr, J. L., Jr., "Perturbation Method for Transonic Flows About Oscillating Airfoils," *AIAA Journal*, Vol. 14, No. 9, 1976, pp. 1258–1265.

[7]Greco, P. C., Lan, C. E., and Lim, T. W., "Frequency Domain Unsteady Transonic Aerodynamics for Flutter and Limit Cycle Oscillation Prediction," AIAA Paper 97-0835, Jan. 1997.

[8]Fung, K. Y., Yu, N. J., and Seebass, R., "Small Unsteady Perturbations in Transonic Flows," *AIAA Journal*, Vol. 16, No. 8, 1978, pp. 815–822.

[9]Bland, S. R., "AGARD Two-Dimensional Aeroelastic Configurations," Rept. AR 156, AGARD, Aug. 1979.

[10]Tijdeman, H., and Schippers, P., "Results of Pressure Measurements on a Lifting Airfoil with Oscillating Flap in Two-Dimensional High Subsonic and Transonic Flow," NLR TR 73018 L, National Aerospace Lab., Amsterdam, The Netherlands, Nov. 1973.

[11]Zwaan, R. J., "NACA 64A006 Oscillating Flap," *Compendium of Unsteady Aerodynamic Measurements*, Rept. R 702, AGARD, Aug. 1982, pp. 1.1–1.15.

[12]Batina, J. T., "Unsteady Transonic Algorithm Improvements for Realistic Aircraft Applications," *Journal of Aircraft*, Vol. 26, No. 2, 1989, pp. 131–139.

[13]Gear, J. A., Ly, E., and Phillips, N. J. T., "Time Marching Finite Difference Solution of the Modified Transonic Small Disturbance Equation," *Proceedings of the 8th Biennial Computational Techniques and Applications Conference*, Australian and Newzealand Industrial and Applied Mathematics, Adelaide, Australia, 1997, pp. 209–216.

[14]Tijdeman, H., "Investigations of the Transonic Flow around Oscillating Airfoils," NLR TR 77090 U, National Aerospace Lab., Amsterdam, The Netherlands, Oct. 1977.

[15]Kwak, D., "Nonreflecting Far-Field Boundary Conditions for Unsteady Transonic Flow Computation," *AIAA Journal*, Vol. 19, No. 11, 1981, pp. 1401–1407.

[16]Seidel, D. A., Bennett, R. M., and Ricketts, R. H., "Some Recent Applications of XTRAN3S," AIAA Paper 83-1811, July 1983.

[17]Ly, E., Gear, J. A., and Phillips, N. J. T., "Improved Approximate Factorisation Algorithm," *Proceedings of the 8th Biennial Computational Techniques and Applications Conference*, Australian and Newzealand Industrial and Applied Mathematics, Adelaide, Australia, 1997, pp. 393–400.

[18]Catherall, D., "Optimum Approximate-Factorization Schemes for Two-Dimensional Steady Potential Flows," *AIAA Journal*, Vol. 20, No. 8, 1982, pp. 1057–1063.

[19]Ballhaus, W. F., Jameson, A., and Albert, J., "Implicit Approximate-Factorization Schemes for the Efficient Solution of Steady Transonic Flow Problems," AIAA Paper 77-634, 1977.

[20]Warming, R. F., and Beam, R. M., "On the Construction and Application of Implicit Factored Schemes for Conservation Laws," *SIAM-AMS Proceedings*, Vol. 11, 1978, pp. 85–129.

[21]Engquist, B., and Osher, S., "Stable and Entropy Satisfying Approximations for Transonic Flow Calculations," *Mathematics of Computation*, Vol. 34, No. 149, 1980, pp. 45–75.

[22]Murman, E. M., "Analysis of Embedded Shock Waves Calculated by Relaxation Methods," *AIAA Journal*, Vol. 12, No. 5, 1974, pp. 626–633.

[23]Ly, E., Gear, J. A., and Hung, H., "Time-Linearised Code for Simulation of Unsteady Transonic Flows over an Aircraft Wing with Moving Shocks," *Proceedings of the 13th Australasian Fluid Mechanics Conference*, Dec. 1998, pp. 567–570.

[24]Ly, E., and Nakamichi, J., "Time-Linearised Transonic Small Disturbance Code Including Entropy and Vorticity Effects," *Proceedings of the 23rd Congress of the International Council of the Aeronautical Sciences* (to be published).

[25]Abbott, I. H., and Von Doenhoff, A. E., *Theory of Wing Sections Including a Summary of Airfoil Data*, Dover, New York, 1959, p. 354.